Available online at www.sciencedirect.com

ScienceDirect

www.elsevier.com/locate/jes

JES JOURNAL OF ENVIRONMENTAL SCIENCES

www.jesc.ac.cn

Distribution and bioavailability of mercury in size-fractioned atmospheric particles around an ultra-low emission power plant in Southwest China

Wei Zhang[1,2], *Jinjuan Li*[1,3,*], *Hao Qiu*[1], *Xingqiang Guo*[1], *Zhijun Fei*[1], *Yi Xing*[4], *Deliang Yin*[3,*]

[1] *College of Resources and Environmental Engineering, Guizhou University, Guiyang 550025, China*
[2] *College of Resources and Environmental Engineering, Guizhou Institute of Technology, Guiyang 550003, China*
[3] *Key Laboratory of Karst Georesources and Environment (Guizhou University), Ministry of Education, Guiyang 550025, China*
[4] *School of Energy and Environmental Engineering, University of Science & Technology Beijing, Beijing 100083, China*

ARTICLE INFO

Article history:
Received 1 November 2022
Revised 21 March 2023
Accepted 22 March 2023
Available online 3 April 2023

Keywords:
Size-fractioned particles
Mercury
Chemical speciation
Coal-fired power plant
Ultra-low emission

ABSTRACT

Ultra-low emission (ULE) technology retrofits significantly impact the particulate-bound mercury (Hg) emissions from coal-fired power plants (CFPPs); however, the distribution and bioavailability of Hg in size-fractioned particulate matter (PM) around the ULE-retrofitted CFPPs are less understood. Here, total Hg and its chemical speciation in TSP (total suspended particles), PM_{10} (aerodynamic particle diameter ≤ 10 μm) and $PM_{2.5}$ (aerodynamic particle diameter ≤ 2.5 μm) around a ULE-retrofitted CFPP in Guizhou Province were quantified. Atmospheric $PM_{2.5}$ concentration was higher around this ULE-retrofitted CFPP than that in the intra-regional urban cities, and it had higher mass Hg concentration than other size-fractioned PM. Total Hg concentrations in PM had multifarious sources including CFPP, vehicle exhaust and biomass combustion, while they were significantly higher in autumn and winter than those in other seasons ($P < 0.05$). Regardless of particulate size, atmospheric PM-bound Hg had lower residual fractions (< 21%) while higher HCl-soluble fractions (> 40%). Mass concentrations of exchangeable, HCl-soluble, elemental, and residual Hg in $PM_{2.5}$ were higher than those in other size-fractioned PM, and were markedly elevated in autumn and winter ($P < 0.05$). In $PM_{2.5}$, HCl-soluble Hg presented a significantly positive relationship with elemental Hg ($P < 0.05$), while residual Hg showed the significantly positive relationships with HCl-soluble Hg and elemental Hg ($P < 0.01$). Overall, these results suggested that atmospheric PM-bound Hg around the ULE-retrofitted CFPP tends to accumulate in finer PM,

* Corresponding authors.
E-mails: summy_lee@163.com (J. Li), dlyin@gzu.edu.cn (D. Yin).

https://doi.org/10.1016/j.jes.2023.03.029

and has higher bioavailable fractions, while has potential transformation between chemical speciation.

Introduction

Atmospheric mercury (Hg) cycling is of globally concerned owing to its long-distance migration and potential risks to public health (Fu et al., 2012; Li et al., 2022). The environmental impacts of atmospheric Hg are controlled by its chemical speciation, which can be operationally divided into gaseous elemental Hg ($Hg^0_{(g)}$), gaseous oxidized Hg ($Hg^{2+}_{(g)}$), and particulate-bound Hg (Hg^P) (Fu et al., 2015). Among these, $Hg^0_{(g)}$ is sufficiently stable to be transported globally, whereas $Hg^{2+}_{(g)}$ and Hg^P have comparatively more local impacts owing to their liable and quick deposition (Zhang et al., 2019a, 2019b). Although Hg^P in the atmosphere accounts only for a lower fraction of less than 10%, its role in the local cycling of atmospheric Hg is more important (Zhang et al., 2019a, 2019b).

Coal-fired power plants (CFPPs) are the major anthropogenic source of atmospheric Hg, and 13.1% of global Hg emissions have been estimated to be from CFPPs (United Nations Environment Programme, 2019). The atmospheric deposition of Hg from CFPPs elevates the Hg levels in the terrestrial system (Fu et al., 2015), and has been found to result in an obvious increase of methylmercury in paddies (Xu et al., 2017). In recent years, the application of ultra-low emission (ULE) technology retrofits comprising electrostatic precipitator (ESP), fabric filter (FF), selective catalytic reduction denitrification (SCR) equipment, and wet flue gas desulfurization (WFGD) system has significantly improved the Hg removal efficiency in China (Wen et al., 2020). However, these devices alter the chemical forms of Hg in the flue and exhaust gases, readily removing oxidized Hg ($Hg^{2+}_{(g)}$) and Hg^P, while still emitting considerable amounts of $Hg^0_{(g)}$ from CFPPs (Li et al., 2019). Recent studies have focused on the impacts of ULE technology retrofits on Hg emissions, speciation transformation and cross-media transfers in CFPPs (Liu et al., 2020; Wen et al., 2020), but comparatively less information is available on the geochemical characteristics of Hg^P around the ULE-retrofitted CFPPs.

Released Hg species such as $Hg^0_{(g)}$ and $Hg^{2+}_{(g)}$ from CFPPs may undergo many reaction processes including $Hg^0_{(g)}$ oxidation and $Hg^{2+}_{(g)}$ reduction, or their gas-particle transformation, which determine their chemical speciation in the atmosphere (Lyman et al., 2020). Released $Hg^0_{(g)}$ can be oxidized to $Hg^{2+}_{(g)}$ by reactive oxygen species, which is then trapped by atmospheric particulate matter (PM) (Lyman et al., 2020). Meanwhile, released $Hg^{2+}_{(g)}$ from CFPPs can be trapped by atmospheric PM. This promotes the formation of Hg^P, and reduces the residence time of atmospheric Hg owing to the higher deposition velocity of Hg^P (Fu et al., 2012; Guo et al., 2021), which may alter the Hg pool and bioavailability in local terrestrial systems. Apart from the contribution of CFPPs, atmospheric Hg^P can be derived from the direct discharge of traffic and residential coal combustion, etc. (Nguyen, 2022; Landis et al., 2007; He et al., 2022; Zou et al., 2022). In addition, the formation of atmospheric Hg^P is also controlled by many influencing factors such as air temperature, air humidity, PM compositions, and PM sizes (Lyman et al., 2020; Gao et al., 2016). However, recent attention related to Hg cycling around CFPPs had mainly been paid to the emission characteristics, chemical transformation in flue gas, and wet/dry deposition (Das et al., 2021; Agarwalla, et al., 2020; Huang et al., 2018), whereas few studies were conducted to determine the geochemical properties of Hg^P around the ULE-retrofitted CFPPs (Gao et al., 2016).

Guizhou Province is one of the major production centers and consumers of coal in China, and its power generation greatly depends on coal combustion. The CFPPs in Guizhou Province have been greatly developed because of the "West-East electricity transmission project" (Tang et al., 2007). However, owing to the special geochemical background, coal mined in Guizhou has substantially higher contents of Hg, ash, and sulfur than that in other areas (Feng and Qiu, 2008). Theoretically, this would significantly elevate the amount of Hg, PM, and sulfate in the atmosphere around the CFPPs, thereby affecting the local cycling of atmospheric Hg (Feng and Qiu, 2008; Liu et al., 2018). In recent years, to conform to the "Reformation and Upgrading Action Plan for Coal Energy Conservation and Emission Reduction" in China, most CFPPs in Guizhou Province have undergone ULE technology retrofits. This would change the concentrations and chemical speciation of atmospheric Hg around the CFPPs, whereas less information can be accessed to date. Then, the investigation of the concentration, distribution, and chemical speciation of Hg in the atmospheric size-fractioned PM around the ULE-retrofitted CFPPs in Guizhou Province could help clarify the special geochemical characteristics.

To achieve this, atmospheric size-fractioned PM including TSP (total suspended particles), PM_{10} (aerodynamic particle diameter $\leq$ 10 μm), and $PM_{2.5}$ (aerodynamic particle diameter $\leq$ 2.5 μm) around a CFPP in Guizhou Province were seasonally collected to analyze the concentration and chemical speciation of Hg. Meanwhile, the environmental risks of Hg^P were also evaluated. The results are expected to provide a knowledge update regarding the geochemical cycling of atmospheric Hg^P around the ULE-retrofitted CFPPs powered by Hg-enriched coal.

1. Methods and materials

1.1. *Site description*

In this study, a ULE-retrofitted CFPP located at Jinsha county (about 6 km away from the Jinsha county center) in Guizhou Province was selected (E 106°15′24″; W 27°28′36″), which is part of the "West-East electricity transmission project" in China.

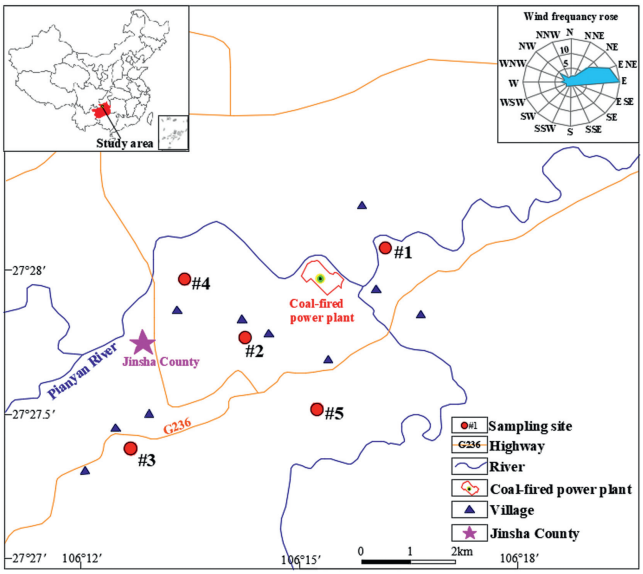

Fig. 1 – Sketch map of studying area and sampling sites (site #1 was the control site located at the upwind direction, while sites #2 and #3 were at the downwind direction (site #3 was adjacent to the river), and sites #4 and #5 were at about 2 km away from the equivalent central site of the four chimneys).

This power plant is equipped with 4 groups of 300 MW coal-fired units, with an annual power generation of approximately 10.5 billion kW/hr and an annual coal consumption of more than 2 million tons. It has 4 chimneys with heights of 245 m and an effective height of 233 m. The boiler comprises a pulverized coal furnace equipped with upgraded air pollution cleaning devices including electrostatic precipitator (ESP), fabric filter (FF), and selective catalytic reduction denitrification (SCR) equipment and wet flue gas desulfurization (WFGD) system. This CFPP is located in the valley of a basin, with low/medium-mountain land formation, and is surrounded by mountains to the north (1048 m above sea level) and south (1057 m above sea level). There are no other large industrial or mining activities in this area, but many residential areas are distributed. The flue gas diffusion from this CFPP is significantly affected by wind direction, terrain, and mountain forests, leading to complex diffusion characteristics compared to those in plain and hilly areas.

Around the CFPP, five sampling sites were selected as determined by the annual wind frequency (Fig. 1). Site #1 (control site) was located upwind of the dominant wind direction, while sites #2 and #3 were located downwind. Sites #1, #2, and #3 were located approximately 1.8, 1.8, and 4.6 km away from a central point, equidistant from the four chimneys, respectively. Especially, site #2 was near the location for the maximum concentration of atmospheric particles predicted by an AERSCREEN model, while site #3 and site #2 were adjoined to the highway and river, respectively. In the non-dominant wind direction, sites #4 and #5 were located approximately 2 km from the equivalent central point. Their spatial distributions are shown in Fig. 1.

1.2. *Samplings*

The sampling campaign was conducted in April, July, October, and January from 2017 to 2018. During each sampling event, TSP, PM_{10}, and $PM_{2.5}$ samples were simultaneously collected within 8-10 days using an intelligent medium-volume sampler (KB-120F, Qingdao Jinshida Electronic Technology Co., Ltd, China) with a flow rate of 100 L/min. A total of 258 samples were collected using quartz filters (WhatmanQMA, φ = 90 mm, pore size = 2.2 μm). Before sampling, the filters were purified at 500°C for more than 1 hr to remove residuary Hg, and weighed by a precision microelectronic analytical balance (XP205, Mettler Toledo International Ltd, Switzerland). For sampling, the samplers were placed at an elevation of approximately 15 m to avoid any sheltering effects. To ensure sample quality, the sampling campaign was stopped if any strong wind, precipitation, or snowfall occurred. The samples were then placed in filter boxes, packed with tinfoil shading, placed in a sealed polyethylene bag, and stored at -4°C.

1.3. *Chemical analysis*

Before chemical analysis, the balanced PM samples were weighed by a precision microelectronic analytical balance (XP205, Mettler Toledo International Ltd, Switzerland) and the PM concentrations were calculated. Total Hg concentrations in the TSP (Hg^P_{TSP}), PM_{10} (Hg^P_{10}), and $PM_{2.5}$ ($Hg^P_{2.5}$) samples were measured according to the methods reported by Qiu et al. (2006) and Gao et al. (2016). Briefly, the quartz filters were cut with a ceramic scissor and digested using a fresh mixture of HNO_3 and HCl (3:1, v/v) in a water bath at 95°C. During digestion, BrCl was added to oxidize all forms of mercury to Hg^{2+}. After digestion for 1.5 hr, ultrapure water was added until a sample volume of 50 mL after the mixed solution had cooled to room temperature, and the mixture was allowed to stand for more than 24 hr. Before determination, 200 μL $NH_2OH{\cdot}HCl$ was added to reduce the excess BrCl. Afterward, $SnCl_2$ was used to reduce the oxidized Hg to Hg^0, which was then trapped by gold dust to form a gold amalgamation. The adsorbed Hg was desorbed via pyrolysis and determined by cold vapor atomic fluorescence spectrometry (CVAFS, MODEL–III, Brooks Rand Co., Ltd, USA) with a detection limit < 0.1 pg.

According to the operational definition of sequential extraction procedures by Xiu et al. (2009), the chemical speciation of Hg in the atmospheric particulates was divided into i) exchangeable particulate mercury (E_XPM), ii) HCl-soluble particulate mercury (HPM), iii) elemental particulate mercury (EPM), and iv) residual particulate mercury (RPM). The analysis method has been detailed by Xiu et al. (2009). Here, some simplified descriptions were listed as followed:

Step 1: One-half of the quartz filters were cut into pieces with ceramic scissors and put into centrifuge tubes. 15 mL $CaCl_2$ (0.1 mol/L) solution was added into the tubes. Then, the samples were treated with ultrasonic waves for 0.5 hr in the ultrasonic machine. After centrifuging for 20 min (4000 r/min), the aqueous phase was determined by CVAFS.

Step 2: 20 mL HCl (1 mol/L) solution and 0.5 mL $CuSO_4$ (1%, w/w) solution were added into the centrifuge tubes used in the previous step. The samples were treated with ultrasonic waves for another 0.5 hr in the ultrasonic machine. After cen-

trifuging for 20 min (4000 r/min), the aqueous phase was determined by CVAFS.

Step 3: 10 mL HNO_3 (2 mol/L) solution was added into the centrifuge tubes used in the previous step. The next steps were the same as above.

Step 4: 10 mL $KMnSO_4$ (5%, w/w) and 5 mL sulfuric acid (1:1, v/v) were added into the centrifuge tubes used in the previous step. Then the tubes were placed in the water bath at 95 ± 2°C for 2 hr. A few drops of hydroxylamine hydrochloride solution (20%, w/w) were added to deplete the residual $KMnO_4$. At last, the aqueous phase was determined by CVAFS.

1.4. Geochemical models of risk assessment

In this study, two geochemical models including the ratio of secondary phase to primary phase mercury (*RSP*) and risk assessment code (*RAC*) based on the chemical speciation in atmospheric PM were conducted to assess the bioavailability and potential hazard of atmospheric Hg^P. The formulas used to calculate the *RSP* and *RAC* are as follows:

$$RAC = (C_i/C_0) \times 100\% \quad (1)$$

where, C_i (μg/g) represents the HPM concentrations in PM, and C_0 (μg/g) represents the Hg^P concentrations (Sakan et al., 2016).

$$RSP = M_{sec}/M_{prim} \quad (2)$$

where, M_{sec} (μg/g) is the Hg concentrations in the secondary phase (Hg in non-residual fraction), and M_{prim} (μg/g) represents the Hg concentrations in the primary phase (Hg in residual fraction) (Liu et al., 2012).

1.5. Quality assurance and quality control

The glassware used in this study was soaked in 20% HNO_3 for 24 hr, cleared with ultrapure water, and then purified at 500°C for 1 hr. Quality assurance and quality control (QA & QC) during chemical analysis were conducted using a method blank, certified reference material (CRM, GSS-5, yellowish red soil, Institute of Geophysical and Geochemical Exploration, Chinese Academy of Geological Sciences, 290 ± 40 ng/g), and sample duplicates. The blank test was conducted at intervals of 10 samples, and their total Hg concentrations were found to be lower than 10 pg, accounting for less than 10% of the measured value in the PM samples.

For total Hg measurement, one parallel was measured for every 5 samples and a CRM test was conducted at intervals of 10 samples. The average recovery ratio and relative standard deviation were 102% and 7%, respectively. For Hg speciation measurement, the ratios of the sum of E_XPM, HPM, EPM, and RPM mass concentration to the total Hg concentration ranged from 90% to 104% in PM, with an average of 98%.

Statistical analysis was conducted using IBM SPSS 25.0 and Origin 8.0 software. The statistical difference analysis and correlation analysis were conducted by one-way ANOVA test and Pearson's correlation coefficient using IBM SPSS 25.0, respectively.

2. Results and discussion

2.1. Distributions of atmospheric PM and Hg^P

2.1.1. Concentrations of atmospheric PM and Hg^P

Daily concentrations of TSP, PM_{10}, and $PM_{2.5}$ ranged from 53.28 to 405.32 μg/m^3, 40.30 to 341.39 μg/m^3, and 37.26 to 206.41 μg/m^3, respectively (Appendix A Table S1). According to Ambient Air Quality Standard in China (GB 3095-2012), 15%, 39%, and 70% of TSP, $PM_{10,}$ and $PM_{2.5}$ samples exceeded their thresholds of 300 μg/m^3, 150 μg/m^3, and 75 μg/m^3, respectively. Moreover, $PM_{2.5}$ concentrations were much higher than that in some coastal cities such as Shanghai, Guangzhou, and Haikou, or inland cities such as Guiyang, Chongqing, and Chengdu (Yin et al., 2017). This result indicates that finer particles ($PM_{2.5}$) are abundant around this CFPP, and a potential health risk for wildlife and humans would occur as they can readily enter the lungs or be adsorbed by foliage (Yin et al., 2017; Lu et al., 2019a, 2019b).

Daily concentrations of Hg^P_{TSP}, Hg^P_{10}, and $Hg^P_{2.5}$ were 54.14-626.97 pg/m^3, 44.64-475.77 pg/m^3, and 40.92-320.16 pg/m^3, with the average values of 262.39, 190.27, and 139.85 pg/m^3, respectively (Appendix A Table S1). $Hg^P_{2.5}$ concentrations were not only significantly lower than those in the urban city at the same geochemical background area (e.g., Guiyang city, 368 ± 676 pg/m^3) (Fu et al., 2011), but also lower than those in the coastal areas (e.g., Shanghai, 300 ± 310 pg/m^3 and Xiamen, 174.4 ± 280.6 pg/m^3) (Duan et al., 2016; Xu et al., 2015). More than that, $Hg^P_{2.5}$ concentrations were still lower than those around the CFPP on the southeast coast of China (309.5 ± 94.9 pg/m^3) (Gao et al., 2016). This may be because the Chinese emission standard of Hg from CFPPs has been restricted to a lower level (less than 30 pg/m^3) (GB 13223-2011) in recent years, while the ULE technology innovations further reduce Hg emissions (Liu et al., 2020). One study found that this CFPP had a relatively lower Hg emission factor (3.87 mg Hg/t coal) than other CFPPs partially because of the synchronous applications of WFGD, ESP, FF, and SCR (Tang et al., 2016). However, the $Hg^P_{2.5}$ concentrations were remarkably higher than those in urban areas in some developed countries such as the United States (8.7 ± 12.8 pg/m^3) (Choi et al., 2013), Republic of Korea (23.9 ± 19.6 pg/m^3) (Kim et al., 2009) and Canada (2.3 ± 3.1 pg/m^3) (Cheng et al., 2013). Meanwhile, they were also remark higher than those around the CFPP in New York, America (8.9 ± 13.5 pg/m^3) (Wang et al., 2013), and slightly higher than the global average concentration (110.6 ± 98.9 pg/m^3) (Zhang et al., 2019a, 2019b) (Fig. 2). Except for the CFPP, vehicle exhaust, and residential coal combustion were prevalent in the studied area, which may synchronously contribute to much atmospheric PM and Hg^P. Such results indicate that although the emissions of CFPPs were well controllable by technological innovations, potential contributions from other sources may be not neglected.

2.1.2. Seasonal distribution of atmospheric Hg^P

Here, the mass and volumetric concentrations, referring to the Hg contents in atmospheric particles per unit mass and unit volume of air, respectively, were used to understand the distribution of atmospheric Hg^P. Compared with the mass

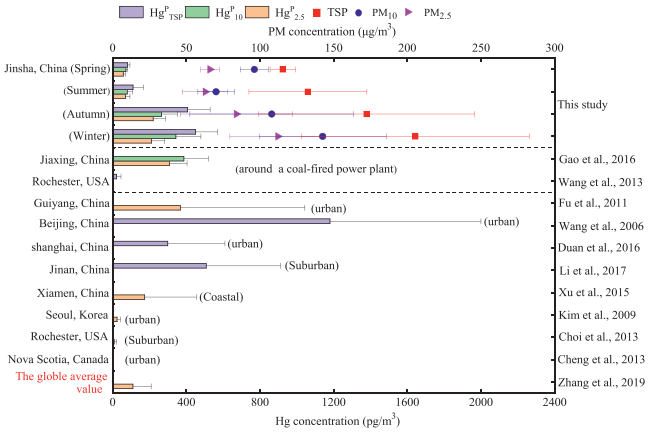

Fig. 2 – Concentrations of Hg in atmospheric size-fractioned particles around the coal-fired power plants, (sub) urban area, or coastal area. The data were collected from global published papers, and represented by average ± standard deviation (AVE ± SD). Hg^P_{TSP}, Hg^P_{10}, and $Hg^P_{2.5}$ represent the total Hg concentrations in the TSP, PM_{10}, and $PM_{2.5}$, respectively.

and volumetric concentrations of Hg^P_{TSP}, Hg^P_{10}, and $Hg^P_{2.5}$ in spring and summer, the concentrations were significantly elevated in autumn and winter, especially in winter ($P < 0.05$, Figs. 2 and 3a), which were consistent with the seasonal distribution of PM. Similar seasonal variations of atmospheric Hg^P were reported in several previous studies (Kim et al., 2012; Fu et al., 2015; Gao et al., 2016). In the studied area, agricultural biomass combustion and residential coal consumption increased substantially in autumn and winter, which may release much humus-enriched PM to bind gaseous Hg, or carry many Hg^P themselves (Wang et al., 2022; Custodio et al., 2020). In addition to emission sources, meteorological conditions such as temperature, precipitation, and wind direction have a more important impact on the atmospheric Hg^P distributions (Fu et al., 2015). Many studies had revealed that low temperature and illumination intensity, fewer precipitation events, or low atmospheric boundary layer during winter could accelerate the accumulation of atmospheric PM, as well as the partitioning of gaseous oxidized Hg or Hg^0 in the atmospheric PM (Guo et al., 2017; Fu et al., 2015; Shanley et al., 2015). Meanwhile, low temperatures also decelerate the volatilization of Hg^0 adsorbed on the PM (Kim et al., 2012). However, we cannot exclude the potential contributions of long-distance transportation as a previous study suggested that cold air from Siberia had an impact on the distribution of atmospheric Hg^P around a CFPP in Xiamen city, China (Huang et al., 2018).

The average Hg mass concentrations in the size-fractioned PM were in the order of $Hg^P_{2.5} > Hg^P_{10} > Hg^P_{TSP}$, while the $Hg^P_{2.5}/Hg^P_{10}$ ratio (122.46% ± 32.88%) was higher than the $PM_{2.5}/PM_{10}$ ratio (79.61% ± 11.81%) (Appendix A Table S1). This result indicates that more Hg^P originates from $PM_{2.5}$ than that from other size-fractioned particles (Sun et al., 2021). Generally, $PM_{2.5}$ has a smaller particulate size and larger specific surface area than PM_{10}, which would provide more adsorption sites for gaseous Hg (Gao et al., 2016). Compared with coarser fractions, fine particles tended to enrich carbonaceous materials (e.g., organic carbon and black carbon) (Wang et al., 2006; Xue et al., 2019), which would provide more chemical ligands competing for gaseous Hg. As the oxidized forms of Hg on the surface of PM are relatively stable, the higher oxidative active fractions (e.g., reactive oxygen species) in $PM_{2.5}$ than those in coarser fractions would increase the oxidation and retention capacities for PM-bound Hg^0 (Styszko et al., 2017). Overall, combined with the higher $PM_{2.5}$ concentrations, it can be concluded that the potential environmental risk of atmospheric Hg^P may be high.

2.1.3. *Spatial distribution of atmospheric PM and Hg^P*

The concentrations of PM and Hg^P at sites #2 and #3 were not only higher than those at the control site (#1) but also higher than those at sites #4 and #5, although there were no significant differences (Fig. 3b). Spatial distributions of PM and Hg^P in this area were possibly co-affected by emission source and wind direction. The highest average concentrations of TSP, PM_{10}, and $PM_{2.5}$ occurred at site #2 (1.8 km away from the CFPP), indicating a direct impact from the CFPP. Nevertheless, Hg^P_{TSP} (324.40 ± 229.33 pg/m³) and Hg^P_{10} (233.30 ± 172.97 pg/m³) reached the highest average concentrations at site #2, while $Hg^P_{2.5}$ presented the highest average level (183.39 ± 140.52 pg/m³) at site #3. This indicates that PM and Hg^P have a spatial mismatch, even though they were closely related ($P < 0.01$). This may be related to the disturbance from the highway less than 100 m from site #3, which discharges vehicle exhaust with substantial fine PM-bound Hg (Nguyen, 2022; Landis et al., 2007). Overall, the formation of PM-bound Hg may be co-controlled by multiple sources, including CFPPs and vehicles, although other sources cannot be excluded.

2.2. *Mercury speciation in atmospheric PM*

2.2.1. *Seasonal distribution of mercury speciation in atmospheric PM*

Considering chemical compositions, E_XPM primarily consists of $CaCl_2$-exchangeable Hg^{2+}, while HPM is mainly composed of a series of oxidized Hg species (e,g., HgO, $HgSO_4$, $HgCl_2$, $HgBr_2$, and HgI_2) (Kim et al., 2012; Xiu et al., 2009). The EPM mainly refers to elemental Hg (Hg^0) adsorbed to the surface of PM by physical mechanisms, which can reflect the contributions of emission sources (Cheng et al., 2017). The RPM may mainly comprise HgS, HgSe, and humus-bound Hg in the core of PM with relatively lower bioactivity, representing the natural sources (Cheng et al., 2017).

Here, we found that ExPM, HPM, EPM, and RPM in size-fractioned PM were significantly elevated in winter and autumn than those in other seasons, regardless of mass or volumetric concentrations (Fig. 4). This was consistent with the seasonal distributions of atmospheric PM (Fig. 2) and Hg^P (Fig. 3a). As mentioned above, increased agricultural biomass combustion and residential coal consumption in autumn and wither would release large amounts of gaseous or PM-bound Hg^0 and Hg^{2+}, which may increase the PM, as well as their bound ExPM, HPM and EPM fractions. Besides, the lower temperature and relatively decreasing height of the atmospheric boundary are conducive to the accumulation of PM. The increase in Hg^P concentration is related to the adsorption of

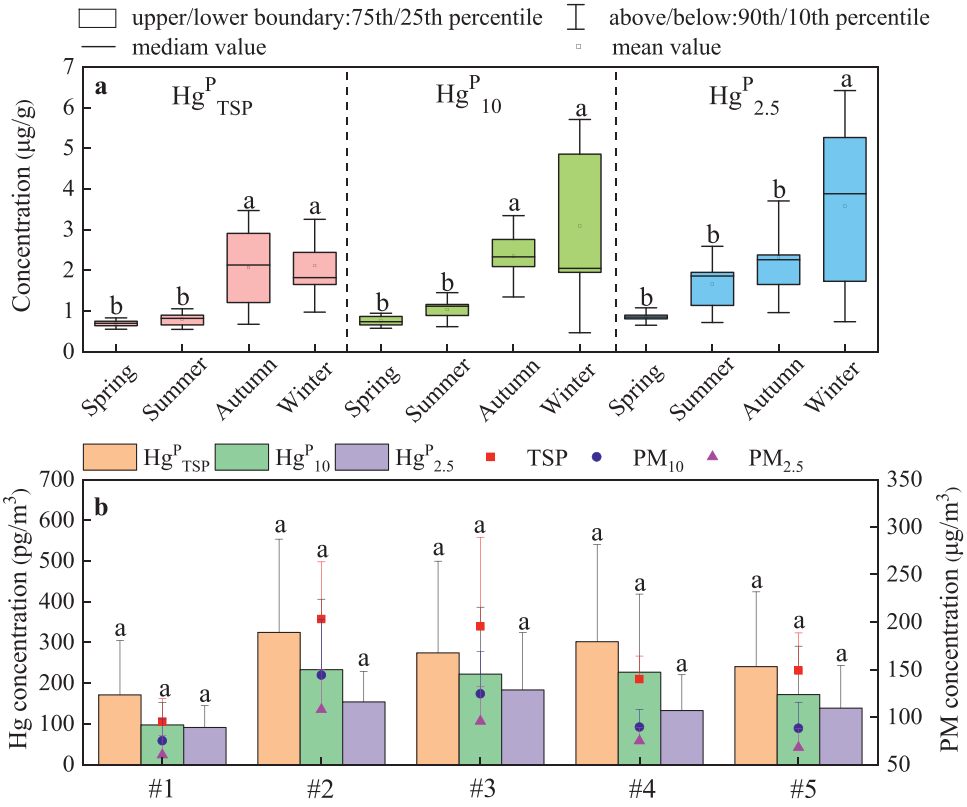

Fig. 3 – (a) Seasonal distribution of mass concentrations of Hg in size-fractioned particles (different lowercase characters represent the statistical difference at significant level, $P < 0.05$) and (b) spatial distribution of volumetric concentrations of size-fractioned particles and their bound Hg (site #1 was the control site, and same lowercase characters represent the statistical difference at no significant level, $P < 0.05$), and the data are represented by AVE ± SD). Hg^P_{TSP}, Hg^P_{10}, and $Hg^P_{2.5}$ represent the total Hg concentrations in the TSP, PM_{10}, and $PM_{2.5}$, respectively.

gaseous Hg^0 and Hg^{2+} by PM. Extremely high $PM_{2.5}$ concentrations (Fig. 2) would also increase the adsorption probability of gaseous Hg^0 and Hg^{2+} in autumn and winter. In addition, low temperatures can synchronously slow down the volatilization of Hg^0 adsorbed on the PM (Kim et al., 2012). Although the formation or source of RPM is currently unclear, which may represent the "inert" Hg species controlling the bioavailability of PM-bound Hg.

However, seasonal distributions of ExPM and HPM were different from the result in previous studies (Gao et al., 2016; Xiu et al., 2009). Their findings showed that higher air temperature, solar radiation and humidity in summer favored the photochemical oxidation of gaseous Hg^0, and thus promoted the formation of E_XPM and HPM (Gao et al., 2016; Xiu et al., 2009). In this study, the average sunshine intensities were 77.2, 133.9, 69.1, and 44.1 W/m^2 in spring, summer, autumn, and winter, respectively. This indicates that the higher E_XPM and HPM concentrations in autumn and winter were less controlled by solar radiation. In autumn and winter, combustion of agricultural biomass and residential coal would not only release large amounts of oxidized Hg species but also increase the products of incomplete combustion such as soot, an important component of $PM_{2.5}$ that potentially produces many hydroxyl radicals (He et al., 2022; Zou et al., 2022). Meanwhile, a greatly high hydroxyl radical oxidation rate in winter has previously been observed, which was comparable to that in summer (Lu et al., 2019a, 2019b). In addition, other oxidants such as ozone, alkyl peroxyl radicals, H_2O_2, NO_3, and halogens may convert Hg^0 to HgO through gas and aqueous phase oxidation reactions, which is the dominant component of HPM (Xiu et al., 2009). This would enhance the conversion of PM-bound or gaseous Hg^0 into oxidized Hg species, which tends to be adsorbed onto PM at a lower temperature, and then increases the E_XPM and HPM fractions (Gao et al., 2016).

2.2.2. *Spatial distribution of mercury speciation in atmospheric PM*

The annual average volumetric and mass concentrations of E_XPM, HPM, EPM, and RPM at sites #2, #3, #4, and #5 were higher than those at control site #1 (Fig. 5). This reveals a potential impact of the CFPP on the local chemical speciation of Hg in PM. Particularly, the annual average mass concentrations of HPM and EPM in the $PM_{2.5}$ were in the order of sites #3 (HPM, 1.28 ± 0.68 μg/g; EPM, 0.63 ± 0.37 μg/g) > site #4 (#5) > site #2 > site #1 (HPM, 0.51 ± 0.29 μg/g; EPM, 0.28 ± 0.14 μg/g). The highest HPM and EPM concentrations at site #3 were consistent with the distribution of $Hg^P_{2.5}$. This may be attributed to the impacts of vehicle exhaust, which can not only release much HPM and EPM but also produce more organic matter in fine PM, trapping more gaseous oxidized Hg and Hg^0 (Landis et al., 2007; Cai et al., 2017; Shen et al., 2021). In addition, the organic matter in $PM_{2.5}$ contributed to the formation of secondary persis-

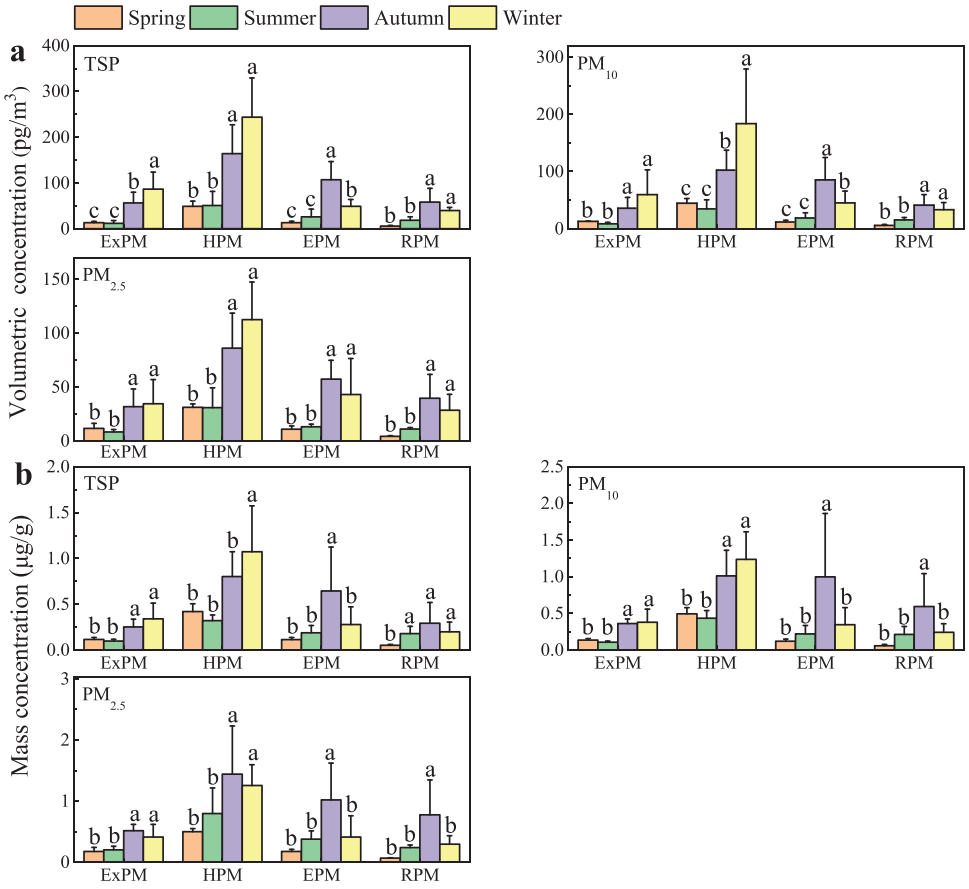

Fig. 4 – (a) Volumetric and (b) mass concentrations of Hg speciation in the atmospheric size-fractioned particles (different lowercase characters represent the statistical difference at significant level, $P < 0.05$), and the data are represented by AVE ± SD).

tent free radicals, which could partially increase the oxidation products of PM-bound Hg^0 (Chen et al., 2019). Interestingly, the annual average mass concentrations of RPM in the $PM_{2.5}$ were higher at sites #4 and #5 (near the rivers) than at other sites. Although we didn't measure the air humidity, it's clear that air humidity is elevated near the rivers, which will be beneficial to the formation of atmospheric aerosol. It is speculated that aerosol fine fractions ($PM_{2.5}$) can facilitate the formation of stable Hg compounds. Nevertheless, this hypothesis is needed to be further certified in the future.

2.3. *Possible chemical transformation of atmospheric Hg^P*

The chemical speciation of Hg in size-fractionated PM can reflect the gas-particle transformation or the sources of Hg, and also affects the bioavailability of atmospheric Hg^P. Based on volumetric concentrations, it was found that PM and PM-bound Hg were highly correlated regardless of particulate sizes ($P < 0.01$), indicating that PM has an important role in the regulation of atmospheric Hg^P pollution. Nevertheless, the mass concentrations of E_XPM, HPM, EPM, and RPM had no relationship with the volumetric concentrations of PM ($P > 0.05$), indicating that atmospheric PM concentrations have a lower impact on the chemical transformation of Hg^P. Furthermore, based on the mass concentration, several relationships between the chemical speciation of Hg in sized-fractioned PM were identified to reveal their sources or transformation mechanisms (Fig. 6).

It was further found that HPM had a significant relationship with ExPM regardless of particle size ($P < 0.01$). This indicates that HPM and E_XPM in finer PM have a similar source of the oxidation of PM-bound Hg^0, or owing to the co-deposition of gaseous oxidized and elemental Hg (Kim et al., 2012). While HPM also showed a significant relationship with EPM ($P < 0.01$) in the $PM_{2.5}$, implying that the adsorption of gaseous Hg and gas-particle transformation of Hg were more likely to occur on fine particles (Gao et al., 2016). In contrast, no relationship between EPM and HPM or E_XPM was observed in the PM_{10} ($P > 0.05$). Meanwhile, the mass concentrations of ExPM, HPM, EPM, and RPM in the $PM_{2.5}$ were higher than those in the PM_{10} (Fig. 5b), suggesting that PM with a smaller size is the key platform for the chemical transformation of PM-bound Hg species or deposition of gaseous Hg species. This may be related to the higher adsorption capacity for gaseous Hg^0 and Hg^{2+}, or the higher oxidative potential of $PM_{2.5}$ than that of PM_{10} (Qie et al., 2018). Hence, the large amounts of gaseous Hg^0 from CFPPs, combined with the comparatively higher atmospheric $PM_{2.5}$ concentrations, may largely increase the production of oxidized Hg species in the atmospheric PM (Fig. 5).

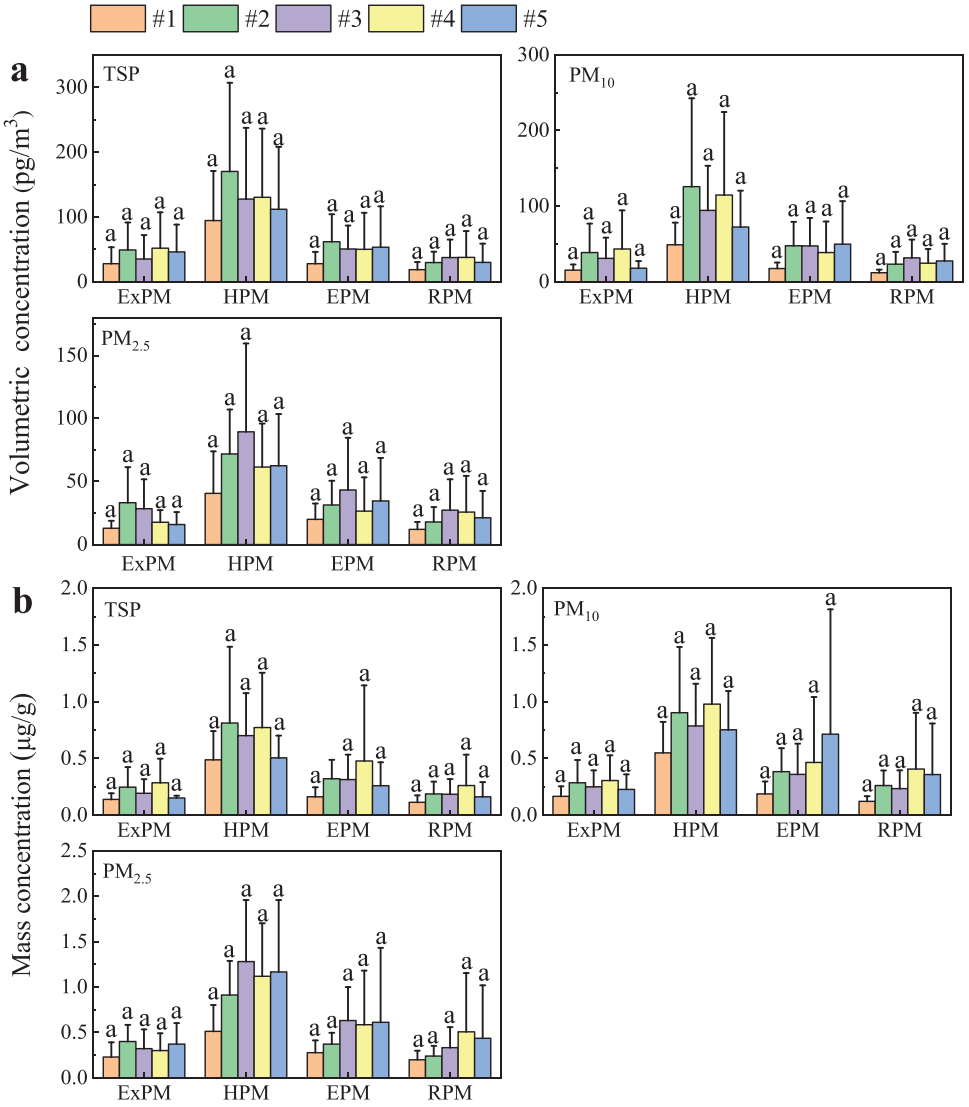

Fig. 5 – Spatial variations of different mercury speciation in the atmospheric size-fractioned particles (different lowercase characters represent the statistical difference at significant level, $P < 0.05$), and the data were represented by AVE ± SD).

The RPM showed a significant relationship with other Hg speciation in the $PM_{2.5}$ ($P < 0.01$), while not in the PM_{10} ($P > 0.05$), indicating their similar sources in the finer particles. Furthermore, a potential transformation between "inert" to "active" fractions in the finer fractions was also possible. The formation of RPM is controlled by the sulfur cycling (organic and inorganic sulfur) in the PM, while the presence of reducible sulfur has been found in the atmospheric PM in previous studies (Longo et al., 2016). In this study, we further found that higher RPM levels in the $PM_{2.5}$ and PM_{10} were found at sites #4 and #5, near the urban rivers, than at other sites (Fig. 6). We thus speculated that these urban rivers contributed to much reducible sulfur (H_2S) to increase the RPM formation (Cruz et al., 2022). Although the potential transformation of PM-bound Hg from "active" to "inert" fractions may occur in the PM, the reversed dissolution from "inert" to "active" components owing to the higher atmospheric sulfate concentrations around the CFPPs cannot be ignored (Chen et al., 2016; Tong et al., 2014). This is partially speculated from the result of higher HPM (e.g., $HgSO_4$) concentrations in this area (Fig. 5).

2.4. *Potential risk of atmospheric Hg^P*

Regardless of particulate sizes, HPM accounted for the highest proportion of total Hg (39.43% ± 4.46% to 59.65% ± 2.56%), remarkably higher than EPM (12.62% ± 6.68% to 31.38% ± 9.96%), E_XPM (11.63% ± 5.57% to 20.19% ± 6.03%), and RPM (7.36% ± 0.32% to 20.63% ± 5.84%) (Table 1). Such a distribution pattern was not consistent with previous research results (Gao et al., 2016; Duan et al., 2016, Cheng et al., 2017; Xiu et al., 2009). In addition, E_XPM accounted for a relatively higher proportion than the result reported in several previous studies (< 2% or lower than the detection limit) (Gao et al., 2016; Duan et al., 2016). And, the HPM proportion in the atmospheric PM was also higher than that in Shanghai (urban city, $PM_{1.6\text{-}3.7}$ < 33% and

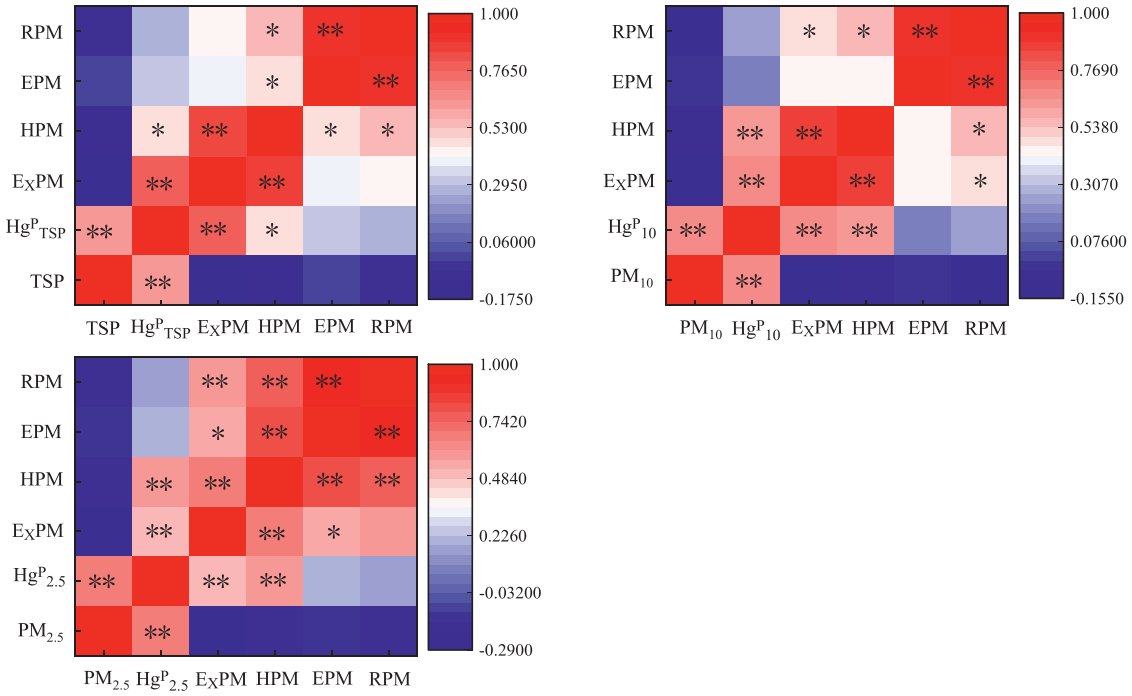

Fig. 6 – Correlations between mercury, mercury speciation and particulate concentrations in size-fractioned particles (*, ** represent the significant levels at 0.05 and 0.01, respectively; Hg^P_{TSP}, Hg^P_{10}, and $Hg^P_{2.5}$ represent the total Hg concentrations in the TSP, PM_{10}, and $PM_{2.5}$, respectively).

Table 1 – Proportion of different mercury speciation to Hg^P in the atmospheric size-fractioned particles.

Content		ExPM	HPM	EPM	RPM
TSP	Spring	16.76% ± 3.35%	59.65% ± 2.56%	16.23% ± 1.13%	7.36% ± 0.32%
	Summer	11.63% ± 5.57%	45.88% ± 8.52%	23.42% ± 4.76%	19.07% ± 8.08%
	Autumn	14.37% ± 3.72%	43.22% ± 12.12%	27.95% ± 8.74%	14.46% ± 5.68%
	Winter	20.19% ± 6.03%	57.23% ± 5.53%	12.62% ± 6.68%	9.96% ± 2.79%
PM_{10}	Spring	17.48% ± 1.98%	59.20% ± 4.43%	15.74% ± 1.97%	7.58% ± 2.68%
	Summer	11.73% ± 2.56%	43.81% ± 8.54%	23.83% ± 6.09%	20.63% ± 5.84%
	Autumn	13.66% ± 4.30%	39.75% ± 7.62%	31.38% ± 9.96%	15.21% ± 2.91%
	Winter	17.05% ± 5.46%	56.72% ± 6.14%	15.44% ± 7.06%	10.79% ± 3.05%
$PM_{2.5}$	Spring	19.35% ± 5.00%	54.57% ± 6.52%	18.70% ± 2.11%	7.38% ± 0.84%
	Summer	13.70% ± 3.01%	45.71% ± 12.38%	21.96% ± 6.11%	18.63% ± 6.01%
	Autumn	15.05% ± 5.08%	39.43% ± 4.46%	28.04% ± 6.91%	17.48% ± 6.31%
	Winter	15.83% ± 7.20%	53.41% ± 7.18%	18.03% ± 6.68%	12.73% ± 1.52%

Hg^P: particulate-bound Hg; TSP: total suspended particles; PM_{10}: aerodynamic particle diameter ≤ 10 μm; $PM_{2.5}$: aerodynamic particle diameter ≤ 2.5 μm; ExPM: exchangeable particulate mercury; HPM: HCl-soluble particulate mercury; EPM: elemental particulate mercury; RPM: residual particulate mercury.

$PM_{3.7\text{-}8}$ < 40%) and Jiaxing (around a CFPP, < 39%) (Xiu et al., 2009; Gao et al., 2016). These results indicated that oxidized Hg fractions in the atmospheric PM are greatly increased around this CFPP. Multiple emission sources, especially the CFPP, can contribute to much gaseous Hg^0, which can be oxidized to gaseous Hg^{2+} by atmospheric oxidizers, and then deposited in the atmospheric PM (Liu et al., 2022). Meanwhile, the adsorbed Hg^0 can be further oxidized to Hg^{2+} by reactive oxygen species in the PM (Styszko et al., 2017; Kim et al., 2012). It may be responsible for the elevated levels of oxidized Hg speciation in the atmospheric PM around the CFPP. Compared with the average RPM proportions in the atmospheric $PM_{2.5}$ in Jiaxing (34.60%, average value calculated by the data in published paper), Shengsi (53.10%), and Shanghai (27.70%) in China (Gao et al., 2016; Cheng et al., 2017; Duan et al., 2016), RPM proportion in this studied area was present at a lower level (< 20%). Among the four Hg components, E_XPM, HPM, and EPM in the atmospheric PM have greater mobility and biogeochemical activity after being deposited into soil or water, which can induce potential environmental risks (Gao et al., 2016). Because of the higher E_XPM and HPM fractions, and the lower RPM fraction, the mobility and biogeochemical activity of atmospheric

Hg^P may be elevated. This could provide much "active" Hg^P in the atmospheric PM, thereby may increase methylmercury production (Zhang et al., 2019a, 2019b). In addition, the deposition of these "active" Hg^P in terrestrial environments such as rice paddies around the CFPPs can enhance their transformation to methylmercury and then induce potential risks (Xiang et al., 2022). This also partially explains the elevated methylmercury production in paddy soils and concentrations of methylmercury in rice (*Oryza sativa* L.) around the CFPP (Xu et al., 2017).

In this study, geochemical models including *RSP* and *RAC* were used to further achieve the bioavailability of atmospheric Hg^P. Although these models are designed to assess the environmental risks of contaminants in soil or sediment, their application to the atmospheric PM may provide some information about the bioavailability of atmospheric Hg^P after entering the terrestrial ecosystems. As shown in Appendix A Table S2, the *RAC* and *RSP* values were from 39.43% ± 4.46% to 59.65% ± 2.56% and 3.72% ± 1.30% to 13.65% ± 4.40%, respectively. According to the risk indexes in Appendix A Table S3, a high risk was concluded, indicating an increased bioavailability of atmospheric Hg^P around the CFPP. No significant difference in *RAC* values between $PM_{2.5}$ and PM_{10} was found, but the values were higher in spring and winter than those in summer and autumn. The *RSP* values also revealed a similar result, indicating the higher bioavailable Hg fractions in the atmospheric PM and elevated potential environmental risks in spring and winter. Overall, the geochemical models reveal an increased bioavailability of atmospheric Hg^P, which can increase the bioavailable Hg pool in the terrestrial systems, as well as the microbial Hg methylation around CFPPs.

3. Conclusions

This study was conducted to understand the distribution and chemical speciation of Hg in the atmospheric size-fractioned PM around a ULE-retrofitted CFPP. Although atmospheric finer PM ($PM_{2.5}$) had high concentrations in this area, their Hg concentrations were relatively low. Concentrations of atmospheric Hg^P in size-fractioned PM in autumn and winter were remarkably higher than those in spring and summer; meanwhile, chemical speciation of PM-bound Hg including ExPM, HPM, EPM, and RPM followed similar results. $PM_{2.5}$ accumulated more Hg and oxidized Hg species (HPM and E_XPM) than other size-fractioned PM. Atmospheric Hg^P and its geochemical forms were co-controlled by emission sources and meteorological conditions. Oxidized Hg speciation (ExPM and HPM) had a clear relationship with particulate-bound Hg^0 (EPM) in the atmospheric PM, and residual Hg likely had a possible transformation mechanism with other Hg speciation in finer PM ($PM_{2.5}$) rather than in coarser PM (PM_{10}). More importantly, potential "active" Hg components such as ExPM and HPM in the atmospheric PM account for a relatively-higher proportion, resulting in high bioavailability and environmental risks of atmospheric Hg^P. This study provides a valuable reference for further understanding the distribution, transformation mechanism, and potential risk of atmospheric Hg^P in size-fractioned PM around ULE-retrofitted CFPPs.

Declaration of competing interest

The authors declare that they have no known competing financial interests or personal relationships that could have appeared to influence the work reported in this paper.

Acknowledgments

This work was supported by the Science and Technology Project of Guizhou Province (No. QKHJC[2020] 1Y187), the National Natural Science Foundation of China (Nos. 41265008, 42007305, and 22166009). We also thank Dr. Zhengcheng Song (Nanjing University) for his manuscript writing guidance.

Appendix A Supplementary data

Supplementary material associated with this article can be found, in the online version, at doi:10.1016/j.jes.2023.03.029.

References

Agarwalla, H., Senapati, R.N., Das, T.B., 2020. Mercury emissions and partitioning from Indian coal-fired power plants. J. Environ. Sci. 100, 28–33.

Cai, T.Q., Zhang, Y., Fang, D.Q., Shang, J., Zhang, Y.X., Zhang, Y.H., 2017. Chinese vehicle emissions characteristic testing with small sample size: Results and comparison. Atmos. Pollut. Res. 8 (1), 154–163.

Chen, Q., Sun, H.Y., Wang, M.M., Wang, Y.Q., Zhang, L.X., Han, Y.M., 2019. Environmentally persistent free radical (EPFR) formation by visible-light illumination of the organic matter in atmospheric particles. Environ. Sci. Technol. 53 (17), 10053–10061.

Chen, X.J., Balasubramanian, R., Zhu, Q.Y., Behera, S.N., Bo, D., Huang, X., et al., 2016. Characteristics of atmospheric particulate mercury in size-fractionated particles during haze days in Shanghai. Atmos. Environ. 131, 400–408.

Cheng, I., Zhang, L., Blanchard, P., Dalziel, J., Tordon, R., 2013. Concentration-weighted trajectory approach to identifying potential sources of speciated atmospheric mercury at an urban coastal site in Nova Scotia. Canada. Atmos. Chem. Phys. 13, 6031–6048.

Cheng, N., Qian, G.L., Duan, L., Zhao, M.F., Xiu, G.L., 2017. Correlation of speciated mercury with carbonaceous components in atmospheric $PM_{2.5}$ in Shengsi region. Environ. Sci. 38 (2), 438–443 (in Chinese with abstract Eglish).

Choi, H.D., Huang, J., Mondal, S., Holsen, T.M., 2013. Variation in concentrations of three mercury (Hg) forms at a rural and a suburban site in New York State. Sci. Total Environ. 448, 96–106.

Cruz, L.P.S., Alves, R.S., Rocha, F.O.C., Moreira, M.S., Júnior, A.S., 2022. Atmospheric levels, multivariate statistical study, and health risk assessment of odorous compounds (H_2S and NH_3) in areas near polluted urban rivers in the city of Salvador, in Northeastern Brazil. Air Qual. Atmos. Hlth. 15, 159–176.

Custodio, D., Ebinghaus, R., Spain, T.G., Bieser, J., 2020. Source apportionment of atmospheric mercury in the remote marine atmosphere: Mace Head GAW station, Irish western coast. Atmos. Chem. Phys. 20, 7929–7939.

Das, T.B., Agarwalla, H., Senapati, R.N., 2021. Mercury emissions and partitioning from Indian coal-fired power plants. J. Environ. Sci. 100, 28–33.

Duan, L., Xiu, G.L., Feng, L., Cheng, N., Wang, C.G., 2016. The mercury species and their association with carbonaceous compositions, bromine and iodine in $PM_{2.5}$ in Shanghai. Chemosphere 146, 263–271.
Feng, X.B., Qiu, G.L., 2008. Mercury pollution in Guizhou, southwestern China - an overview. Sci. Total Environ. 400 (1–3), 227–237.
Fu, X.W., Feng, X.B., Qiu, G.L., Shang, L.H., Zhang, H., 2011. Speciated atmospheric mercury and its potential source in Guiyang, China. Atmos. Environ. 45 (25), 4205–4212.
Fu, X.W., Feng, X.B., Sommar, J., Wang, S.F., 2012. A review of studies on atmospheric mercury in China. Sci. Total Environ. 421-422, 73–81.
Fu, X.W., Zhang, H., Yu, B., Wang, X., Lin, C.–J., Feng, X.B., 2015. Observations of atmospheric mercury in China: a critical review. Atmos. Chem. Phys. 15, 9455–9476.
Gao, J.Y., Wang, H., Cai, W., Wu, J.T., He, Y.F., 2016. Pollution characteristics of atmospheric particulate mercury near a coal-fired power plant on the southeast coast of China. Atmos. Pollut. Res. 7, 1119–1127.
Guo, J.M., Kang, S.C., Huang, J., Zhang, Q.G., Rupakheti, M., Sun, S.W., et al., 2017. Characterizations of atmospheric particulate-bound mercury in the Kathmandu Valley of Nepal, South Asia. Sci. Total Environ. 579, 1240–1248.
Guo, J.M., Sharma, C.M., Tripathee, L., Kang, S.C., Fu, X.W., Huang, J., et al., 2021. Source identification of atmospheric particle-bound mercury in the Himalayan foothills through non-isotopic and isotope analyses. Environ. Pollut. 286, 117317.
He, G.Z., Ma, J.Z., Chu, B.W., Hu, R.Z., Li, H., Gao, M., et al., 2022. Generation and Release of OH Radicals from the Reaction of H_2O with O_2 over Soot. Angew. Chem. Int. Ed. 61, 1–4.
Huang, S.Y., Sun, L.M., Zhou, T.J., Yuan, D.X., Du, B., Sun, X.W., 2018. Natural stable isotopic compositions of mercury in aerosols and wet precipitations around a coal-fired power plant in Xiamen, southeast China. Atmos. Environ. 173, 72–80.
Kim, P.R., Han, Y.J., Holsen, T.M., Yi, S.M., 2012. Atmospheric particulate mercury: concentrations and size distributions. Atmos. Environ. 61, 94–102.
Kim, S.H., Han, Y.J., Holsen, T.M., Yi, S.M., 2009. Characteristics of atmospheric speciated mercury concentrations (TGM, Hg (II) and Hg (p)) in Seoul. Korea. Atmos. Environ. 43, 3267–3274.
Landis, M.S., Lewis, C.W., Stevens, R.K., Keeler, G.J., Dvonch, J.T., Tremblay, R.T., 2007. Ft. McHenry tunnel study: Source profiles and mercury emissions from diesel and gasoline powered vehicles. Atmos. Environ. 41 (38), 8711–8724.
Li, Y.X., Wang, Y., Li, Y., Li, T., Mao, H.T., Talbot, R., et al., 2017. Characteristics and potential sources of atmospheric particulate mercury in Jinan. China. Sci. Total Environ. 574, 1424–1431.
Li, Z.G., Chen, X.F., Liu, W.L., Li, T.S., Chen, J., Lin, C.J., et al., 2019. Evolution of four-decade atmospheric mercury release from a coal-fired power plant in North China. Atmos. Environ. 213, 526–533.
Li, Z.G., Huang, Y.M., Liu, J.L., Sun, G.Y., Wang, Q.F., Xiao, H.X., et al., 2022. Mass flow, enrichment and potential environmental impacts of mercury in a preheater-precalciner cement plant using multiple mining and industrial wastes. J. Environ. Manage. 311, 114819.
Liu, C., Fu, X.W., Xu, Y., Zhang, H., Wu, X., Sommar, J., et al., 2022. Sources and transformation mechanisms of atmospheric particulate bound mercury revealed by mercury stable isotopes. Environ. Sci. Technol. 56, 5224–5233.
Liu, F., Hu, J.W., Huang, X.F., Chen, J.G., Fu, L.Y., Luo, J., 2012. Assessment of heavy metals pollution in sediments from Aha Lake. China. Adv. Mater. Res. 554-556, 1913–1918.
Liu, K.Y., Wang, S.X., Wu, Q.R., Wang, L., Ma, Q., Zhang, L., et al., 2018. A highly resolved mercury emission inventory of Chinese coal-fired power plants. Environ. Sci. Technol. 52 (4), 2400–2408.
Liu, S.T., Hao, H.K., Jia, W.B., Cao, Y., Chen, C.M., 2020. Effects of ultralow-emission retrofitting on mercury emission from a coal-fired power plant. Energ. Fuel. 34 (6), 7502–7508.
Longo, A.F., Vine, D.J., King, L.E., Oakes, M., Weber, R.J., Huey, L.G., et al., 2016. Composition and oxidation state of sulfur in atmospheric particulate matter. Atmos. Chem. Phys. 6, 13389–13398.
Lu, K.D., Fuchs, H., Hofzumahaus, A., Tan, Z.F., Wang, H.C., Zhang, L., et al., 2019a. Fast photochemistry in wintertime haze: consequences for pollution mitigation strategies. Environ. Sci. Technol. 53 (18), 10676–10684.
Lu, X.C., Lin, C.Q., Li, W.K., Chen, Y.A., Huang, Y.Q., Fung, J.C.H., et al., 2019b. Analysis of the adverse health effects of $PM_{2.5}$ from 2001 to 2017 in China and the role of urbanization in aggravating the health burden. Sci. Total Environ. 652, 683–695.
Lyman, S.N., Cheng, I., Gratz, L.E., Weiss–Penzias, P., Zhang, L.M., 2020. An updated review of atmospheric mercury. Sci. Total Environ 707, 135575.
Nguyen, L.S.P., Hien, T.T., Truong, M.T., Chi, N.D.T., Sheu, G–R., 2022. Atmospheric particulate-bound mercury (PBM_{10}) in a Southeast Asia megacity: Sources and health risk assessment. Chemosphere 307, 135707.
Qie, G.H., Wang, Y., Wu, C., Mao, H.T., Zhang, P., Li, T., et al., 2018. Distribution and sources of particulate mercury and other trace elements in $PM_{2.5}$ and PM_{10} atop Mount Tai, China. J. Environ. Manage. 215, 195–205.
Qiu, G.L., Feng, X.B., Wang, S.F., Shang, L.H., 2006. Environmental contamination of mercury from Hg-mining areas in Wuchuan, northeastern Guizhou, China. Environ. Pollut. 142, 549–558.
Sakan, S., Popović, A., Anđelković, I., Đorđević, D., 2016. Aquatic sediments pollution estimate using the metal fractionation, secondary phase enrichment factor calculation, and used statistical methods. Environ. Geochem. Health. 38 (3), 855–867.
Shanley, J.B., Engle, M.A., Scholl, M., Krabbenhoft, D.P., Brunette, R., Olson, M.L., et al., 2015. High mercury wet deposition at a "clean air" site in Puerto Rico. Environ. Sci. Technol. 49 (20), 12474–12482.
Shen, X.B., Hao, J.T., Kong, L., Shi, Y., Cao, X.Y., Shi, J.C., et al., 2021. Variation characteristics of fine particulate matter and its components in diesel vehicle emission plumes. J. Environ. Sci. 33 (9), 138–149.
Styszko, K., Samek, L., Szramowiat, K., Korzeniewska, A., Kubisty, K., Rakoczy-Lelek, R., et al., 2017. Oxidative potential of PM_{10} and $PM_{2.5}$ collected at high air pollution site related to chemical composition: Krakow case study. Air Qual. Atmos. Hlth. 10 (9), 1123–1137.
Sun, L.M., Zhang, X.D., Zheng, J.Y., Zheng, Y.Q., Yuan, D.X., Chen, W.J., 2021. Mercury concentration and isotopic composition on different atmospheric particles (PM_{10} and $PM_{2.5}$) in the subtropical coastal suburb of Xiamen Bay, Southern China. Atmos. Environ. 261, 118604.
Tang, L., Liu, H.Y., Feng, X.B., Li, Z.G., Fu, C.C., Wang, H., et al., 2016. Mercury emissions from a coal-fired power plant burning high ash content anthracite. Chinese J. Ecol. 35 (5), 1351–1357 (in Chinese with abstract Eglish).
Tang, S.L., Feng, X.B., Qiu, J.R., Yin, G.X., Yang, Z.C., 2007. Mercury speciation and emissions from coal combustion in Guiyang, Southwest China. Environ. Res. 105 (2), 175–182.
Tong, Y.D., Eichhorst, T., Olson, M.R., Rutter, A.P., Shafer, M.M., Wang, X.J., et al., 2014. Comparison of heterogeneous photolytic reduction of Hg (II) in the coal fly ashes and synthetic aerosols. Atmos. Res. 138, 324–329.
United Nations Environment Programme, 2019. Global mercury assessment 2018. Available: https://wedocs.unep.org/20.500.11822/27579. Accessed September 10, 2022.

Wang, X., Chen, Y.K., Guo, X., Dai, W.T., Liu, Y.L., Wu, F., et al., 2022. Saccharides in atmospheric $PM_{2.5}$ in tropical forest region of southwest China: Insights into impacts of biomass burning on organic carbon aerosols. Chemosphere 308, 136251.

Wang, Y.G., Huang, J.Y., Hopke, P.K., Rattigan, O.V., Chalupa, D.C, Utell, M.J., et al., 2013. Effect of the shutdown of a large coal-fired power plant on ambient mercury species. Chemosphere 92, 360–367.

Wang, Z., Zhang, X., Chen, Z., Zhang, Y., 2006. Mercury concentrations in size-fractionated airborne particles at urban and suburban sites in Beijing, China. Atmos. Environ. 40, 2194–2201.

Wen, M.N., Wu, Q.R., Li, G.L., Wang, S.X., Li, Z.J., Tang, Y., et al., 2020. Impact of ultra-low emission technology retrofit on the mercury emissions and cross-media transfer in coal-fired power plants. J. Hazard. Mater. 396, 122729.

Xiang, Y.P., Guo, Y.Y., Liu, G.L., Liu, Y.W., Song, M.Y., Shi, J.B., et al., 2022. Particle-Bound Hg(II) is available for microbial uptake as revealed by a whole-cell biosensor. Environ. Sci. Technol. 56 (10), 6754–6764.

Xiu, G.L., Cai, J., Zhang, W.Y., Zhang, D.N., Büeler, A., Lee, S.C., et al., 2009. Speciated mercury in size-fractionated particles in Shanghai ambient air. Atmos. Environ. 43 (19), 3145–3154.

Xu, L.L., Chen, J.S., Yang, L.M., Niu, Z.C., Tong, L., Yin, L.Q., et al., 2015. Characteristics and sources of atmospheric mercury speciation in a coastal city, Xiamen, China. Chemosphere 119, 530–539.

Xu, X.H., Meng, B., Zhang, C., Feng, X.B., Gu, C.H., Guo, J.Y., et al., 2017. The local impact of a coal-fired power plant on inorganic mercury and methyl-mercury distribution in rice (Oryza sativa L.). Environ. Pollut. 223, 11–18.

Xue, H.Q., Liu, G.J., Zhang, H., Hu, R.Y., Wang, X., 2019. Similarities and differences in PM_{10} and $PM_{2.5}$ concentrations, chemical compositions and sources in Hefei City, China. Chemosphere 220, 760–765.

Yin, D.Y., Zhao, S.P., Qu, J.J., 2017. Spatial and seasonal variations of gaseous and particulate matter pollutants in 31 provincial capital cities, China. Air Qual. Atmos. Hlth. 10, 359–370.

Zhang, H., Fu, X.W., Wang, X., Feng, X.B., 2019a. Measurements and distribution of atmospheric particulate–bound mercury: a review. Bull. Environ. Contam. Toxicol. 103, 48–54.

Zhang, H., Wang, Z.W., Zhang, X.S., 2019b. Methylmercury concentrations and potential sources in atmospheric fine particles in Beijing, China. Sci. Total Environ. 681, 183–190.

Zou, D.L., Sun, Q.Q., Liu, J.S., Xu, C., Song, S., 2022. Seasonal source analysis of nitrogen and carbon aerosols of $PM_{2.5}$ in typical cities of Zhejiang, China. Chemosphere 303, 135026.